

The Physics of MRI Safety

Lawrence P. Panych, PhD^{1,2*} and Bruno Madore, PhD^{1,2}

The main risks associated with magnetic resonance imaging (MRI) have been extensively reported and studied; for example, everyday objects may turn into projectiles, energy deposition can cause burns, varying fields can induce nerve stimulation, and loud noises can lead to auditory loss. The present review article is geared toward providing intuition about the physical mechanisms that give rise to these risks. On the one hand, excellent literature already exists on the practical aspect of risk management, with clinical workflow and recommendations. On the other hand, excellent technical articles also exist that explain these risks from basic principles of electromagnetism. We felt that an underserved niche might be found between the two, ie, somewhere between basic science and practical advice, to help develop intuition about electromagnetism that might prove of practical value when working around MR scanners. Following a wide-ranging introduction, risks originating from the main magnetic field, the excitation RF electromagnetic field, and switching of the imaging gradients will be presented in turn.

Level of Evidence: 5

Technical Efficacy: 1

J. MAGN. RESON. IMAGING 2018;47:28–43.

While it is from the nucleus of the hydrogen atom that a solitary proton's spin provides the source of the magnetic resonance imaging (MRI) signal, the operation of the MRI scanner itself can be thought of as orchestrating a complex dance of electrons. A torrent of them rushes forward, round and round, in the coils of the main magnet while jets of them streak back and forth in the gradient and RF coils. Each electron generates a field around itself, to inform the Universe about how everything with electrical charge should interact with it. As electrons dance, their fields coax nuclear spins into an unsteady gyration of their own and the MRI signal is created. The present article is about this electromagnetic dance and how people can get hurt when it goes wrong.

As the tag “magnetic” in the name announces, an MRI scanner is very much about magnetism. Three different types of coils and the magnetic fields they generate are involved in creating images. First, there is the so-called “main magnet,” which produces the large static magnetic field. This is most often a superconducting electromagnet but it could also be a permanent magnet. Added to this is a coil to generate the radiofrequency electromagnetic field (the “RF field”) and, lastly, there are the imaging gradient coils, responsible for creating the spatial-encoding magnetic

fields and typically referred to as “the gradients.” While essential in allowing the MRI device to produce images, these coils and the manner in which the fields they generate interact with matter can also, at times, be the cause of serious threats to human life and limb.^{1–10}

This article explores the physics underlying the safety risks associated with the three principal types of coils and magnets. A number of other reviews and exposés exist that cover the basic physics behind the interactions of one or more of these and are recommended as supplemental reading.^{11–20} For those who wish to go even deeper into the physics, excellent basic textbooks exist on electromagnetism^{21,22} and the magnetic properties of materials.²³ Good intuition on the interactions between electromagnetic fields and materials can be obtained through numerical simulation of Maxwell's equations, the fundamental equations that govern these interactions. For this we recommend a nice book by Elsherbeni and Demir²⁴ that comes complete with well-documented MatLab code (MathWorks, Natick, MA).

There are a dozen equations in this article. Of these, two of Maxwell's equations and the Lorentz force equation provide the mathematical basis for the physical interactions considered. The others, which we find useful for back-of-the-envelope calculations, are meant to help the reader gain

View this article online at wileyonlinelibrary.com. DOI: 10.1002/jmri.25761

Received Feb 9, 2017, Accepted for publication Apr 24, 2017.

*Address reprint requests to: L.P.P., 75 Francis St., Boston, MA 02115. E-mail: panych@bwh.harvard.edu

From the ¹Department of Radiology, Brigham and Women's Hospital, Boston, Massachusetts, USA; and ²Harvard Medical School, Boston, Massachusetts, USA

intuition about these interactions, in particular, with respect to size and degree. How strong is the magnetic force? How much will the RF field heat the tissue? How much current will be induced in a conductor? We aim at giving some feeling for the degree to which a particular interaction might represent a hazard, and in this sense, we hope this article may prove useful.

The static magnetic field

The “main magnet” of a commercial MRI system is the most distinguishing feature of the device, and also the greatest source of risk. The field it generates, typically about 1.5–3.0T, is much stronger than magnetic fields casually encountered in everyday life; for example, it is roughly 30,000–60,000 times the average of the Earth’s magnetic field at the surface and is roughly 300–600 times stronger than the field of a common refrigerator magnet. Because MRI involves field strengths much beyond typical everyday experience, regular objects may behave in a nonintuitive manner near scanners. How objects behave in such conditions greatly depends on what they are made of, and for this reason we will begin by looking at the magnetic properties of materials. For objects most affected by magnetic fields, we will consider the translational and rotational forces acting on them. We will also take a cursory look at the effect of the scanner’s static field on biological processes, and the effects of motion in such an environment.

Susceptibility and the Magnetic Properties of Materials

The volume magnetic susceptibility of a material expresses the degree to which a material becomes magnetized in response to an external magnetic field. It is commonly represented by the dimensionless scalar, X_v or just X , which will be used throughout this article. In many crystals, X may have to be represented in a more complicated manner—as a tensor—but here it is just a number, ie, a scalar. The magnetization of a material is simply XB_o , where B_o is the magnitude of the external magnetic field. Values of X for elements of the periodic table have been tabulated and are readily available from online sources.²⁵

Materials can be classified according to their magnetic properties, and there are three main types of materials, depending on whether X is large and positive, small and positive, or small and negative. The first category, large and positive, represents ferromagnetic materials and is the only category causing safety concerns in the presence of B_o , the MR’s large static magnetic field. At room temperature, only a few elements such as iron, nickel, and cobalt exhibit ferromagnetic properties. Of these, iron is the most widespread, and for this reason iron-containing objects are typically the culprits for projectile incidents at MRI sites. While all materials are to some extent magnetized when subjected to a

large magnetic field, ferromagnetic materials are distinguished in that, under the right circumstances, the magnetic dipoles of every molecule in the material can come into alignment, resulting in a very large local magnetic field. In other words, ferromagnetic materials can become magnetically saturated.

Most everyday objects that do not contain iron would fit in the latter category, having small and negative magnetic susceptibility. Such materials are called diamagnetic and include common items such as water, wood, many types of plastics, and almost all biological tissues. The negative sign associated with their magnetic susceptibility means that such materials are (ever so slightly) repelled by a magnet. This fact has been demonstrated, most dramatically, by levitating frogs.²⁶

The third type of material, with small and positive magnetic susceptibility, is referred to as paramagnetic. Although not particularly common in everyday life, paramagnetic materials such as solutions of chelated gadolinium and manganese play an important role in the design of chemical contrast agents in MRI, while the paramagnetism of deoxyhemoglobin is central to the endogenous blood oxygenation level-dependent (BOLD) contrast exploited in functional MRI. Chemical contrast agents and their safety is a topic deserving an article on its own, beyond the scope of the present one.

In the next two sections we will look at the translational and torsional forces exerted on ferromagnetic objects due to B_o . Paramagnetic and diamagnetic materials also experience these forces; however, they are generally too small to be of practical importance. Because iron is such a prevalent metal it might be easy at times to develop the impression that all metallic objects must be ferromagnetic; in contrast, metals such as copper and many types of stainless steel are essentially nonmagnetic, for example. Assuming they are pure enough, objects made of these nonmagnetic metals do not cause any projectile risk in an MR environment. That said, and given the prevalence of iron in everyday objects, suspicion of all metals and testing with a hand-held magnet remains a healthy reflex.

Translational Forces Due to Interaction With a Static Magnetic Field

Ferromagnetic objects are attracted to magnets, so logically, the closer one such object gets to an MRI scanner the stronger the attraction should grow, should it not? Actually, no; in fact, a ferromagnetic object at the center of the bore would feel no attraction at all, and maximum force would instead be felt somewhere outside the scanner. This is one example of nonintuitive behavior, further explained below.

As a rule of thumb, whenever magnetic forces are significantly less than the gravitational pull on the same object,

then the magnetic forces should cause no major safety concern.^{27,28} In other words, the weight of an object will be used below as a reference, to help provide an understanding of how strong magnetic forces may be. The computation of forces and torques can be very complicated because they depend on the strength of the magnetic field and of its spatial gradient, as well as the exact composition and geometry of the object submitted to it. While a more thorough discussion of this topic can be found elsewhere,¹⁷ the text below aims at providing intuition about the forces at play.

The spatial gradient of the B_o field is a key parameter determining the force exerted on an object. The spatial gradient is simply the change in the strength of the magnetic field with respect to distance and is measured in Tesla per meter (T/m) or, alternatively, in Gauss per centimeter (G/cm) (1 T/m = 100 G/cm). The “grad” operator “ ∇ ,” as in ∇B_o , takes the spatial derivative of B_o and thus captures how quickly B_o varies spatially. More specifically, ∇B_o is a vector field, which means that every point in space is associated with a vector. Note that, in this paper, bold face type is used to indicate a vector. Consider one such point in space: at this selected location, ∇B_o would provide a vector whose length represents how steeply B_o is changing at that location, and whose orientation would point in the direction of steepest change.

Another key quantity that describes the magnetism of the object brought into the B_o field is the magnetic dipole, which is represented here by the vector μ_m . The dipole is often represented as a current loop enclosing some small region, thus explaining its units of measure—amperes times meters-squared (Am²). While the dipole itself has no actual spatial extent, it does have in the space around it an associated magnetic field equal to the field that would be generated by such a current loop. Figure 1 shows a schematic of an idealized magnetic dipole and its magnetic field profile.

The main parameter of interest in the present section is the translational magnetic force, F_{trans} , exerted on an object as its dipole interacts with the field.^{23,29,30} A relation for F_{trans} can be derived by calculating the Lorentz force (discussed later) due to B_o acting on the current loop that is assumed to generate the magnetic dipole³⁰:

$$F_{trans} = \mu_m \cdot \nabla B_o \tag{1}$$

where the dot product of two vectors as used in Eq. 1 is a scalar with a magnitude equal to the product of the lengths (magnitudes) of the two vectors times the cosine of the angle between them. To make Eq. 1 a little more intuitive, will be put in relation to the gravitational force on the same object, F_g . Assuming that μ_m is aligned with ∇B_o , we then obtain an equation for the ratio of F_{trans} to F_g that will prove useful in estimating the degree to which a magnetic field can pull on objects:

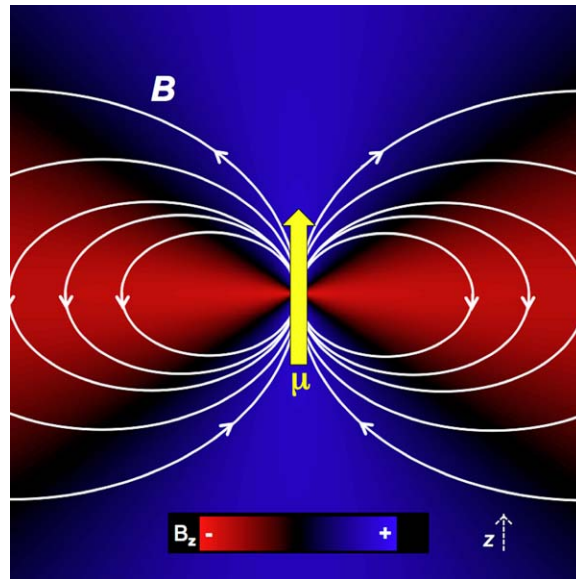


FIGURE 1: The drawing shows a schematic representation of the B field lines for a single magnetic dipole, μ . In the blue region, the B_z component of the dipole field is in the positive z -direction so that magnetic material in this region will be encouraged to align in the same direction as the dipole, ie, become magnetized. In the red region, the B_z component of the dipole field is opposite the dipole orientation and magnetic material in this region will tend to align opposite the dipole, ie, become demagnetized. A short, flat object with little to no extent in the z -direction would tend to have a large demagnetizing field because it would mostly fall into red-labeled space. In contrast, a tall, slender object oriented along z would have a minimum demagnetizing field.

$$\frac{F_{trans}}{F_g} = CX B_o |\nabla B_o|, \quad C = \frac{1}{(\mu_o g) \rho} \tag{2}$$

In Eq. 2, X is the magnetic susceptibility of the material, and $|\nabla B_o|$ at any given point is the length of the vector ∇B_o at that point. In the definition of the constant, C (which is approximately equal to 10 m/T² for ferromagnetic metals), μ_o is the permeability of free space, g is the gravitational acceleration constant, and ρ is the material density. Note that F_{trans}/F_g depends on $B_o |\nabla B_o|$, often referred to as the spatial gradient product (SGP). Equation 2 is independent of how much material there is; while a larger object would lead to a stronger magnetic force F_{trans} , it would also be heavier, leaving F_{trans}/F_g unchanged.

In practice, Eq. 2 is mostly applicable for materials with very small susceptibilities, ie, for materials whose magnetism is always very small compared to the externally applied field. It requires some adjustment when dealing with ferromagnetic objects. While the term $X B_o$ in Eq. 2 represents the strength of the magnetic flux as created within the object, such flux could not grow to arbitrarily large levels even if B_o were to grow arbitrarily large. Instead, it would plateau once a maximum value is reached. This maximum is the saturation flux density, B_s . For a given ferromagnetic material, the internal magnetic flux cannot grow

beyond B_s regardless of how large B_o might become. For this reason, Eq. 2 is only valid wherever XB_o is less than B_s , which tends to be true for all realistic values of B_o as far as diamagnetic and paramagnetic materials are concerned, but not so for ferromagnetic materials. For example, in nickel, X is around 600 and B_s is 0.64 T; thus, Eq. 2 is only appropriate wherever B_o remains below 1.1 mT. Wherever the material is saturated, Eq. 2 should therefore be modified as follows:

$$\frac{F_{trans}}{F_g} = C B_s |\nabla B_o|, \text{ (saturated ferrmagnetic objects)} \quad (3)$$

B_s in ferromagnetic objects may range from about 0.25–2.5 T, with nickel at about 0.64 T and iron at about 2.5 T.

Based on Eq. 3, one can estimate how strongly a scanner may pull on ferromagnetic objects in its vicinity. The maximum spatial gradient on some modern MRI systems can exceed 10 T/m and, accordingly, from Eq. 3, magnetic forces on objects made of nickel or iron can readily reach 60 or 250 times their weight, respectively. Even for a modest one-pound iron object, one can appreciate how magnetic forces can readily become superhuman in nature, and that no amount of “holding on tight” to an object might come close to matching them. Such a force is enough, for example, to accelerate an iron object to a speed of 200 km/h in less than 25 milliseconds.

Even when ferromagnetic objects are not saturated, it turns out that Eq. 2 is still not of much practical use. This is because the magnetization of ferromagnetic objects very much depends on their shape, a fact that Eq. 2 does not take into account. As the microscopic domains of ferromagnetic materials become aligned with B_o , their strong magnetic dipole fields overlap so as to partly cancel each other, effectively reducing the magnitude of X . Alternatively, one may think of the induced magnetic field of the material as having a component that opposes the applied field, referred to as the demagnetizing field.²³ The demagnetizing field undermines the work of B_o as it tries to magnetize the material, effectively reducing the susceptibility.

Figure 1 may help to demonstrate the idea of the demagnetizing field. The magnetic field of a single dipole oriented in the z -direction is shown schematically by the white streamlines in the figure. Locations where the z -component of the dipole field is positive are marked in blue, and magnetic material in this region will be encouraged to align in the same direction as the dipole, ie, to become magnetized. In contrast, wherever the z -component of the dipole field is negative, as highlighted with red in Fig.1, magnetic materials tend to align opposite the dipole, ie, to become demagnetized. A flat object with almost no extent in the z -direction would have a large demagnetizing field (see red region in Fig. 1), while a slender object aligned

along z might be associated with a negligible demagnetizing field (see blue region in Fig. 1). In general, for arbitrarily-shaped ferromagnetic objects, determining the details of this demagnetizing field can be very complex and requires the use of numerical methods.

For some simple object geometries, a shape-dependent demagnetization factor can be introduced to account for the effects of the demagnetizing field. In this case, Eq. 2 is modified by replacing X with $X/(1+DX)$ to give the following:

$$\frac{F_{trans}}{F_g} = C \frac{X}{(1+DX)} B_o |\nabla B_o|, \text{ (non saturated ferromagnetic objects)} \quad (4)$$

where D is the demagnetization factor, which takes on values between 0 and 1. Strictly speaking, Eq. 4 assumes the object to be an ellipsoid of revolution (ie, created by rotating an ellipse about one of its two axes), with the axis of revolution aligned along B_o (see expression for F_z in Ref. 17 with $\theta = 0$). For very long and slender needle-like objects, D approaches 0 and $X/(1+DX) \approx X$, meaning that Eq. 4 becomes equivalent to Eq. 2. For less needle-like ferromagnetic objects, because $X \gg 1$, $X/(1+DX) \approx 1/D$, a number much smaller than X . Consider a few examples involving simply-shaped objects oriented in particular ways with respect to B_o . For a sphere, D equals 1/3 and therefore the effective susceptibility is just 3, irrespective of the actual magnitude of X . With a long needle-like object oriented perpendicular to B_o , D equals 1/2 and the effective susceptibility is 2. Likewise, for a thin plate or film parallel to B_o , D is equal to 0, but if the plate is perpendicular to B_o , then D is equal to 1.

Overall, for ferromagnetic objects, one should use Eq. 4 up to $B_o = DB_s$, whereupon Eq. 4 will give the same force ratio as Eq. 3. From this point onward, as one gets closer to the scanner, the object is fully saturated and Eq. 3 should be employed. Note that Eq. 3 does not involve D , meaning that once close enough to a scanner for the object to become saturated, shape would have little effect on translational pull.

Consider the example of a sphere made of nickel; with $D=1/3$ and $B_s=0.64$ T. As it approaches the scanner, Eq. 4 would remain valid up to $DB_s \approx 0.2$ T. However, if the same piece of nickel were long and slender instead and pointed in the same direction as B_o , for example with $D=1/30$, then Eq. 4 would be valid only up to 0.02 T. In other words, the long and slender object would saturate more easily so that the full force described in Eq. 3 would become applicable even further away from the scanner. In contrast, although hardly advisable, one could walk up a little closer to the scanner with the spherically-shaped object in hand while still remaining under the more lenient rule of Eq. 4, until saturation is reached and Eq. 3 would be brought to bear upon the object.

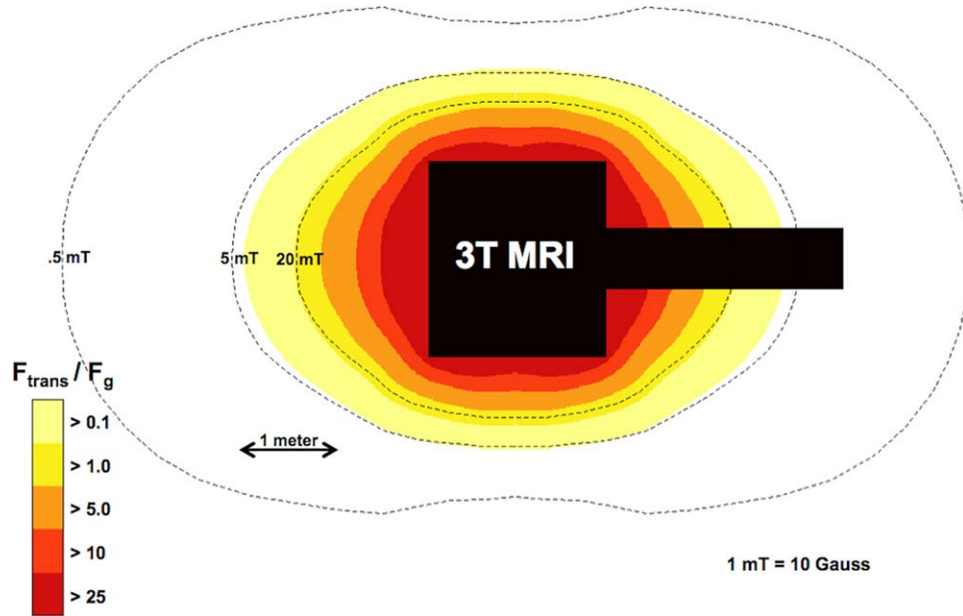


FIGURE 2: Regions of different force ratios, F_{trans}/F_g , were computed for an actively shielded, 3T clinical MRI system. Magnetic field and spatial gradient data were derived from line plots in manufacturer data sheets and interpolated to compute force ratios using Eqs. 3 and 4, assuming $C = 10 \text{ m/T}^2$, $D = 0.01$, and $B_s = 2.5 \text{ T}$. The field lines for .5 mT, 5 mT, and 20 mT (5, 50, and 200 Gauss) are shown for reference.

Maximal translational forces occur at a location just outside the bore where spatial gradients, $|\nabla B_o|$, tend to be the greatest. Inside the bore, as one nears isocenter, the field becomes very uniform and $|\nabla B_o| = 0$, meaning that F_{trans} also becomes zero there. Active shielding in modern scanners allows the field to be better contained and scanners to be sited in smaller rooms, but they also tend to make $|\nabla B_o|$ much larger, as the field must transition from nearly zero to full strength in a shorter distance. As a result, from the perspective of Eqs. 1–4, dynamic shielding actually makes scanners more dangerous by increasing the magnetic translational forces involved.

Figure 2 demonstrates the application of Eqs. 3 and 4 for a typical shielded 3T MRI system, for an elongated ($D = 0.01$) iron object ($B_s = 2.5 \text{ T}$) pointed toward the scanner, showing the force ratio, F_{trans}/F_g , for locations around the scanner. It should be noted how, in less than a meter, the ratio may grow from less than 1, which may not be dangerous, to above 10, where the situation can rapidly become unmanageable and all bets are off. In specific locations, translational forces reach well over a hundred times the object’s weight (not shown). For the scanner in Fig. 2, the region roughly between the 5 and 20 mT lines (50 and 200 Gauss) demarcates a zone where anyone bearing a ferromagnetic object might want to do some deep thinking about the wisdom of advancing further.

Torque Due to Interaction With a Static Magnetic Field

In addition to the translational force that moves ferromagnetic objects along the spatial gradient of the magnetic field,

there can also be significant torque applied to objects with highly asymmetric shapes, such as long cylinders or ellipsoids. Mathematically, the torque on a dipole μ_m in a magnetic field B is equal to the vector product of μ_m and B (see Ref. 23, page 51):

$$T = \mu_m \times B \tag{5}$$

where T is the torque. The vector (or cross) product of two vectors is also a vector. Its orientation is orthogonal to the original two vectors and its magnitude is equal to the product of their lengths times the sine of the angle between them.

Note how the expression for T in Eq. 5 differs from the expression for F_{trans} in Eq. 1 in the sense that maximum torque occurs where the strength of the B_o field itself is maximum rather than where its spatial gradients are maximum. For this reason, maximum torque typically occurs inside the MRI’s bore. For small asymmetrically shaped ferromagnetic objects implanted in the body, the torquing force may be the dominant safety issue (rather than the translational force), as discussed below.

Let us define a force, F_{torque} , as the restraining force one would have to apply to the two ends of a ferromagnetic, elongated object (eg, an ellipsoid of revolution with the length several times the width) to prevent it from rotating and lining up with the field. To make this more intuitive, the force might be put in relation with the translational force, F_{trans} , on the same object.¹⁷ More specifically, the ratio between the maximal values of both of these forces is given below. Of course, the maximal values of these

forces do not occur at the same location in/around the scanner as F_{torque}^{max} occurs near isocenter, while F_{trans}^{max} occurs near the entry to the bore. Even so, the ratio between the two forces can help one understand the importance of torqueing as a safety issue, particularly for small implants. We find that,

$$\frac{F_{torque}^{max}}{F_{trans}^{max}} = \frac{(B_o)_{max}}{L|\nabla B_o|_{max}}, \text{ (saturated elongated object)} \quad (6)$$

where L is the length of the object. As an example, taking typical values for a 3T shielded MRI system with a maximum spatial gradient of 10 T/m, and assuming $L=1$ cm, we find from Eq. 6 that the force one needs to apply to the ends of the object to prevent torqueing in the magnetic field can reach 30 times the maximum translational force. Thus, especially in the case of an elongated object implanted into the body, potential damage from torqueing can readily become a greater source of concern than translational forces.

It may seem at first somewhat counterintuitive that for an object of greater length (larger L in Eq. 6) the F_{torque}^{max} is reduced compared to F_{trans}^{max} . Consider, however, that for a constant torque the force required to prevent turning decreases the further one is from the axis of rotation: for example, it is much easier to loosen a bolt with a long-handled wrench than it is with a short one. Similarly, for a given torque, it would be more difficult for surrounding tissues to prevent a small clip from twisting compared to a longer one.

Direct Interactions Between the Static Magnetic Field and Living Tissue

For currently available clinical MRI systems, magnetic translational forces and torques on diamagnetic and paramagnetic tissues have been estimated and shown to be much too small to be of any safety concern. For example, the tendency of iron-containing red blood cells to separate from plasma due to the differential translational force (ΔF_{trans}) based on the susceptibility difference of the tissues (ΔX) can be calculated. If one assumes a relatively high but realistic SGP of 25 T²/m and in Eq. 2 replaces X with ΔX and ρ with $\Delta\rho$, the difference in density between red blood cells and plasma, then ΔF_{trans} is found to be less than 8% of the difference in gravitational pull (ΔF_g) on the tissues.¹⁷ Although, one finds for the SPG of 1400 T²/m that was sufficient to levitate frogs (which admittedly is not a very realistic SPG for a practical human-sized MRI), the ΔF_{trans} would be more than 400% of ΔF_g . Accordingly, any human willing and able to share in the frog's exhilarating experience of magnetic levitation might also partly separate their red blood cells from plasma in the process, with unknown health effects.

More immediate concerns regarding the interaction of living tissues with the magnetic fields of actual MRI systems in use today involve vertigo and nausea, two well-documented and unpleasant effects on the vestibular system caused by motion in the static magnetic field. Whether these vestibular symptoms may be caused by magnetic forces, for example, those resulting from anisotropic susceptibility or from the magnetohydrodynamic effect (discussed below), or whether they may be related to induced currents associated with motion in the magnetic field still remains unclear.¹⁹

Another potential force effect comes from current-carrying tissue structures being physically pulled one way or another by the Lorentz force. As charged particles move in a magnetic field, a force emerges that is perpendicular to both the direction of motion and the field:

$$\mathbf{F}_L = q(\mathbf{v} \times \mathbf{B}) \quad (7)$$

where q is the charge of the particle, \mathbf{v} is its velocity, and \mathbf{F}_L is the Lorentz force. The magnitude of the Lorentz force on current-carrying metal conductors can be significant, as will be discussed in the section on gradients. However, currents in biological tissues such as nerves are generally found to be too small to be of any practical concern even at field strengths as high as 20T.³¹

The Lorentz force acts on all charged particles in motion, and these particles may sometimes take the form of ions (ie, charged molecules) in a flowing liquid. Such interactions fall under the general category of magnetohydrodynamics and the effects in the body have been studied extensively.³²⁻³⁴ Blood flowing in a direction orthogonal to a magnetic field experiences a reverse pressure impeding the flow, but this is expected to result in an insignificant increase in blood pressure even in a high-field MRI.^{32,33} Of greater practical concern is that positive and negative ions in blood are pushed in opposite directions by the Lorentz force, causing a charge separation and an electric field that corrupts electrocardiograms and complicates the task of performing cardiac-gated MRI.³⁵⁻³⁷

It is well known that movement in a magnetic field can induce a voltage (due to Faraday's law of induction, discussed in more detail later) in electrically conductive materials, including biological tissues, especially when the motion is through regions of space where the magnetic field changes steeply. For example, near the entry to the bore of a 3T MRI where $|\nabla B_o|$ tends to be greatest, it can be shown that current densities over 0.1 A/m² may be produced in conductive tissues due to the voltage induced by normal movement.^{38,39} This is more than twice the 0.04 A/m² (low frequency) limit for exposure of workers recommended by the International Commission for Non-Ionizing Radiation Protection (ICNIRP).⁴⁰ Whether or not one considers the

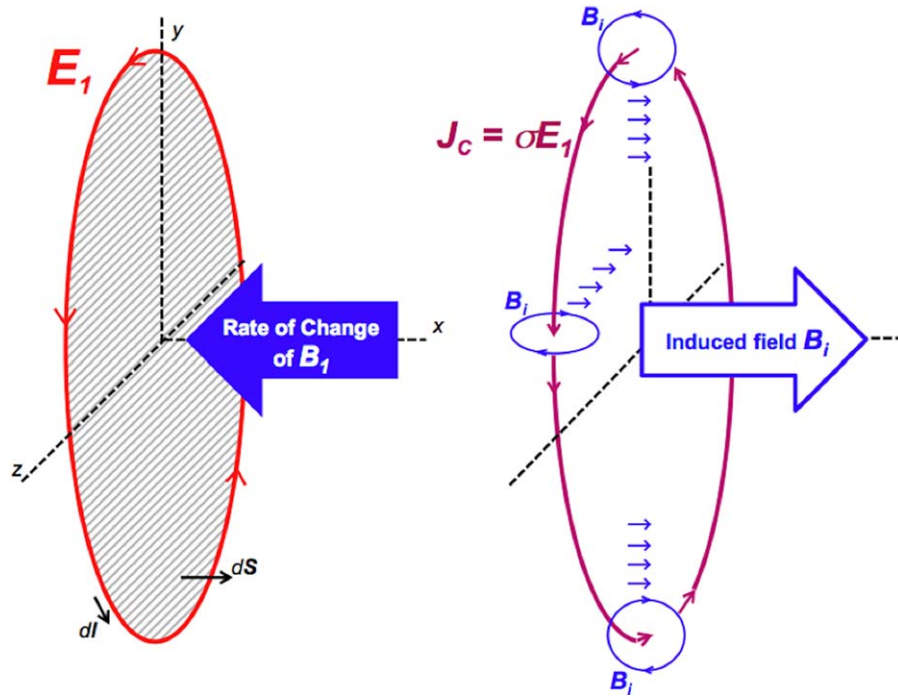


FIGURE 3: Left: Schematic demonstrating Faraday’s law whereby an electric field is generated such that the electromotive force or voltage around a closed loop or contour is proportional to the time rate of change of the magnetic flux density integrated over the enclosed surface. Note that $d\mathbf{l}$ is a unit vector tangent to the contour at any point along its length and $d\mathbf{S}$ is a unit vector normal to the enclosed surface. The electric field orientation lies in a plane perpendicular to the direction of B_1 . In a conducting medium, this electric field generates eddy currents in the same orthogonal plane. Right: Schematic demonstrating the effect of Ampere’s law, whereby a magnetic field, B_i , is induced by currents, including by the eddy currents generated by Faraday induction.

ICNIRP limit as overly conservative, currents induced in tissue deserve serious attention as a potential MRI safety concern, especially as new high-field MRI systems are introduced. Further, because the magnitude of the induced current is proportional to conductivity, significant current densities may also be generated in metals used in implants. For example, currents induced in metallic heart valves have been studied over such concerns.^{41,42}

The RF Field

The magnetic field generated by the RF coil excites nuclear spins to produce MRI signals. Compared to the main B_0 field, which is strong and static, the magnetic field component of the transmitted RF field (often referred to as B_1) is weak and varies rapidly in time, oscillating at the Larmor frequency, which is equal to γB_0 , (where γ is 42.577 MHz/T for hydrogen) and is about 128 MHz at 3T. The maximum strength of B_1 is only a few microTesla (μT), an order of magnitude lower than the Earth’s magnetic field at the surface and many orders of magnitude smaller than B_0 . However, even though the B_1 field is small in magnitude, its high frequency leads to safety concerns.

RF Heating of Biological Tissue

The field produced by the RF coil deposits energy into the body in the form of heat: currents are induced in the electrically conductive biological tissues and heating occurs due

to resistance to the current. The problem of heating due to the use of the RF coil can be acute when metallic implants are present, as will be discussed in a later section.

The Maxwell-Faraday equation is directly relevant when considering interactions with the RF field. It is written as follows:

$$\oint_c \mathbf{E} \cdot d\mathbf{l} = - \int_S \frac{\partial \mathbf{B}}{\partial t} \cdot d\mathbf{S}, \quad (8)$$

where the field \mathbf{B} considered here is the magnetic field generated by the RF coil, B_1 . Equation 8 expresses the fact that an electric field is generated such that the electromotive force or voltage around a stationary closed loop (integral of \mathbf{E}) is equal to (the negative of) the time rate of change of the magnetic flux density integrated over the surface enclosed by the loop. This is shown schematically by the drawing on the left of Fig. 3. Note that, as shown in Fig. 3, $d\mathbf{l}$ is a unit vector tangent to the contour at any point along its length and $d\mathbf{S}$ is a unit vector normal to the enclosed surface at any point on the surface. The plane of orientation of the generated electric field (and therefore the plane of circulation of eddy currents generated in a conductive medium) is perpendicular to the direction of B_1 ; for example, it would be in a sagittal plane if B_1 were oriented left–right in the scanner.

In the case of heating, it is not directly the transmitted B_1 that causes problems, but rather the associated electric

field, represented by \mathbf{E}_1 in Fig. 3. In a conductive medium, \mathbf{E}_1 drives a conduction current density equal to $\sigma\mathbf{E}_1$, where σ is the conductivity of the medium. The instantaneous rate of energy dissipated per unit volume (power density) due to resistance to this current is $\sigma|\mathbf{E}_1|^2$ W/m³. Dividing by the mass density of the medium gives the mean power deposition per kg, which is referred to as the specific absorption rate (or SAR):

$$\text{SAR} = \sigma E_p^2 / 2\rho \text{ (Watts/kg)} \quad (9)$$

where ρ is the mass density (1.06×10^3 kg/m³ in muscle) and E_p is the peak amplitude of the time-varying (and sinusoidal) \mathbf{E}_1 . Dividing the SAR by the heat capacity of tissue, which is around 4200 J/kg/°C, one obtains the rate at which tissue is expected to heat if there was no mechanism for cooling. For example, a SAR of 4.2 Watts/kg will heat tissues at a rate of 10^{-3} °C per second. A volume of tissue subjected to this power deposition will be heated 1°C (the FDA exposure limit) in 1000 seconds, or about 17 minutes, again assuming there is no cooling during this period.

In order to meet regulatory requirements, it is necessary to measure or calculate the SAR for MRI pulse sequences. A rough estimate of the SAR at the surface of the body may be obtained using a simple loop model.¹¹ Based on Eq. 8, in a surface ring of tissue of radius, R , exposed to uniform RF field, an electric field would be generated in the loop with peak magnitude as follows:

$$E_p = \pi f B_p R \quad (10)$$

where f is the Larmor frequency (in Hz) and B_p is the peak amplitude of the magnetic field component of the electromagnetic field produced by the RF coil. Combining Eqs. 9 and 10:

$$\text{SAR} = (\sigma/2\rho) (\pi f B_p R)^2 \quad (11)$$

Equation 11 is the usual expression for SAR, as widely published and employed. It is useful in the sense that it shows some important trends such as that SAR increases with the square of both f and B_p . A rough calculation assuming $\sigma = 0.5$ S/m, $f = 128$ Mhz (for a 3T system), a body radius of 20 cm, with $B_p = 2$ μ T, gives a SAR of about 6.5 W/kg, which is well over the 4 W/kg FDA limit for whole body absorption. However, the value calculated above is the local (and maximum) SAR at the body periphery. The average SAR will be less than half of this. In addition, it should be noted that we have implicitly assumed a duty cycle of 100% in this calculation. A reduction in duty cycle with the same B_p will give a proportional reduction in SAR.

Overall, the assumption that Eq. 10 gives the true value of E_p (and thus Eq. 11 gives the true SAR) is reasonably accurate for low-frequency excitations (eg, below 10

MHz). Simulations reveal, however, that even at a frequency of 42.58 MHz, the Larmor frequency at 1T, the estimate of the magnitude of the electric field based on Eq. 10 is not accurate. Why is this?

Looking back at Eq. 8, we are reminded that the oscillating \mathbf{B}_1 field generated by the RF coil induces an electric field, \mathbf{E}_1 , and, in a conducting medium, a circulating conduction current density equal to $\sigma\mathbf{E}_1$. This induced current in turn generates a new magnetic field, as we will see from another of Maxwell's equations, Ampere's law, which further connects \mathbf{E} and \mathbf{B} as follows:

$$\oint_c \mathbf{B} \cdot d\mathbf{l} = \iint_s \mu \mathbf{J} \cdot d\mathbf{S}, \quad \mathbf{J} = \mathbf{J}_C + \mathbf{J}_D = \sigma\mathbf{E} + \epsilon \frac{\partial \mathbf{E}}{\partial t} \quad (12)$$

where \mathbf{J}_C and \mathbf{J}_D are the conduction and displacement current densities, respectively. Equation 12 expresses the fact that a magnetic field is generated around a closed loop proportional to the sum of the total current passing through the surface enclosed by the loop. Ampere's law applies to all currents and, as shown schematically by the drawing on the right side of Fig. 3, this also includes those eddy currents generated through Faraday induction that were discussed previously. Thus, there is a new induced \mathbf{B}_i field that combines with the original source RF field and, because of this, the magnitude of the generated electric field no longer has a simple dependence on B_p (defined as the magnitude of the transmitted RF only). The importance of the induced magnetic field component increases with increasing frequency.

It is possible to combine both the Maxwell equations and solve them analytically to obtain more accurate \mathbf{E} field and SAR values¹¹; however, this can only be done for homogeneous media in simple geometries such as spheres and cylinders and with an ideal distribution of RF irradiation. While solutions involving these simple models may be useful in elucidating the basic behavior of electromagnetic waves in conductive tissue, they are limited when it comes to obtaining direct answers as to what SAR can be expected for a human MRI exam. For this, numerical methods, which are not constrained to solving for simple geometries in homogeneous media, are typically employed.⁴³ A good general discussion of the use of numerical field calculations for MRI safety applications can be found in Refs. 44–46 and with respect to the RF field specifically in Ref. 47.

Obtaining accurate SAR estimates in vivo is especially complicated by the fact that the human body has a complex geometry and is not uniform in terms of its electrical properties.⁴⁸ Conductivities, for example, can vary by as much as an order of magnitude between tissue types. Attempts have been made to develop human body models that, when used with numerical simulation techniques, may give accurate estimates of SAR.^{49–56} A more direct and potentially more accurate approach to estimate SAR is to use actual MRI

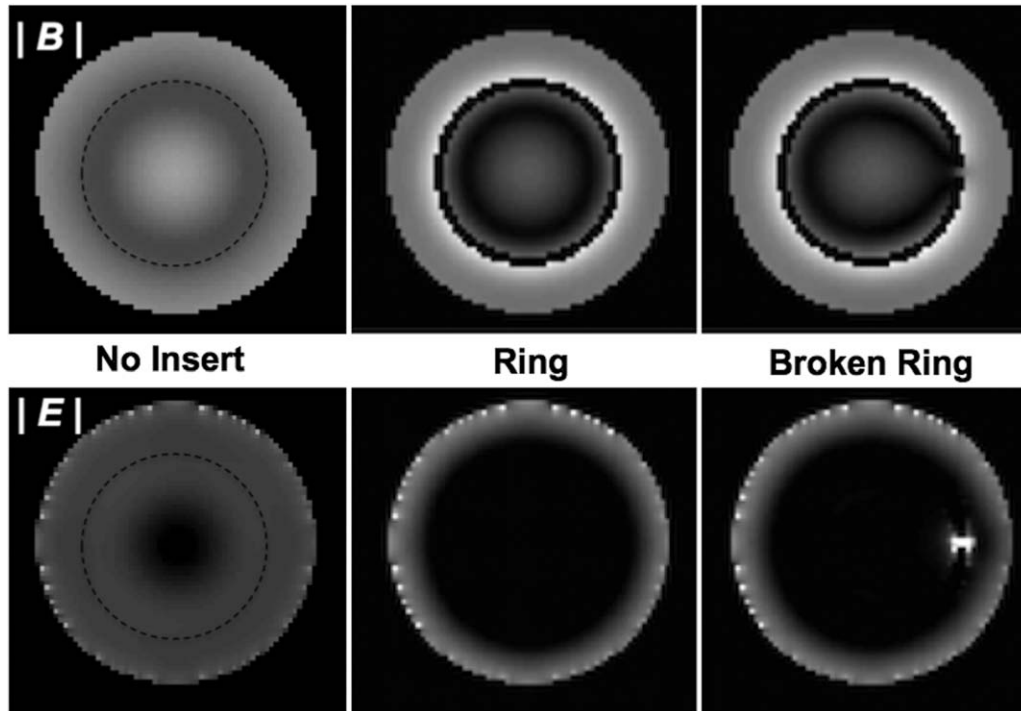


FIGURE 4: Simulated magnitude of E and B fields in the sagittal plane (y - z) due to a 128 MHz uniform B_1 excitation in the x -direction. The field calculations were based on a finite-time finite-difference simulation in a uniform conductive cylinder of a material with electrical properties similar to biological tissues ($\sigma = 0.5$ S/m, $\epsilon_r = 80$, $\mu_r = 1$). Images in the left column involve only tissues, no metal implant. A dashed circle shows the location where a metallic ring was introduced, with results shown in the middle column. For images in the right column a small gap was introduced into the metal ring. SAR is caused by the electric field, not directly by the magnetic field, and for this reason the E field as shown in the bottom row is of special interest. Note how the insertion of the ring in the central column did not lead to any increase in electrical field (and SAR). But the insertion of a small gap in the loop dramatically increased the electrical field in the right column, potentially leading to significant heating and burns.

images; for example, obtaining B_1 maps that may then be used to estimate the E field and derive the SAR distribution.^{57–60}

It is important to note that, for the purposes of safety monitoring, SAR is merely used as a surrogate measure for the potential to cause tissue damage. The real problem is heating. Numerical models that use SAR, not as the endpoint, but as input to estimate resultant temperature changes in the body via, for example, the Pennes bioheat transfer equation, have been employed to this end.^{61–66} An even more direct means of determining the likelihood of tissue damage is to obtain in vivo temperature maps through MR-based temperature mapping using the fact that the water resonant frequency is temperature-dependent.^{67–71}

RF Interaction With Metallic Objects Forming Loops

As long as MRI equipment is functioning properly and limits regarding SAR are respected, no dangerous heating should occur during routine MRI as a result of RF irradiation. It is still possible, however, to cause serious tissue damage when conductive metallic objects are present. Currents generated by the RF field in these objects do not significantly affect global SAR, but they can focus energy deposition in small volumes and create localized tissue damage.

Let us consider a copper loop placed perpendicular to the RF field orientation and look at Eq. 11, which was used when estimating the SAR of a ring of tissue. The conductivity of copper is about 8 orders of magnitude higher than that of biological tissues, and its density is close to 10 times that of tissue; accordingly, from Eq. 11, the SAR in the metal would be around 10 million times greater than in tissue and one would expect enormous heating. The fact is, however, that there is actually very little heating of the metal.⁷² How can this discrepancy be explained?

As detailed in the previous section, Eq. 11 is only an approximation, and it cannot be applied to situations where currents are large (whether due to high f , or the presence of highly conductive metal). The heating predicted by Eq. 11 does not happen because Eq. 12, again, comes into play. The current in the loop will itself generate a magnetic field that will counter the driving B_1 field. If the current induced in the loop grows large enough to generate a field that exactly cancels B_1 , then no more current can be induced. Figure 4, which shows the magnitudes of the B and E fields under different simulated situations, illustrates this fact. The magnitude of the E field is shown on the bottom left of Fig. 4, for a section of conductive tissue-like material irradiated by a uniform 128 MHz B_1 field oriented perpendicular to the section. The magnitude of the E field pattern shows

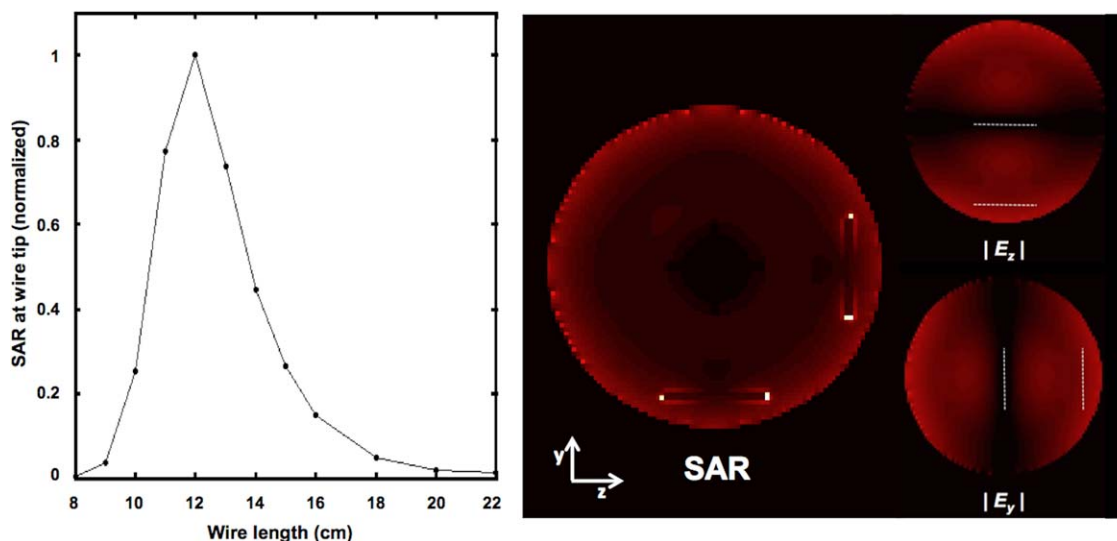


FIGURE 5: Results of simulations with thin (insulated) wires placed in a uniform B_1 field of 128 MHz. The field calculations were based on a finite-time finite-difference simulation in a uniform conductive cylinder of a material with electrical properties similar to biological tissues ($\sigma = 0.5$ S/m, $\epsilon_r = 80$, $\mu_r = 1$). The plot on the left shows the estimated SAR for wires of varying length. As expected, the peak SAR occurred at 12 cm, the half wavelength value. The center image is the estimated SAR with 12-cm wires placed in the cylinder at four different positions. The position of the four wires is indicated by dashed white lines in the images on the right. Simulations involved a single wire at a time, and the center image is a composite rendering of four separate simulations. Note how wires at the center of the object caused minimal SAR elevation. The explanation for this fact can be seen in the images on the right, showing how the y and z components of the electrical field vanished at the center. In contrast, wires near the periphery of the object caused marked SAR increases, especially near the tips of the wires.

a radial dependence on intensity, as expected from Eq. 10. Note that the B field is no longer uniform due to the contribution from the field generated by the circulating currents.

At the center of Fig. 4 the magnitudes of the B and E fields are shown for the case when a conductive metal ring is placed inside the tissue. The B inside the ring almost completely disappears and the E field is totally suppressed as well. Not only is there minimal SAR within the metal ring itself (and thus no risk of dangerous heating), but the ring essentially acts as a shield to limit SAR for tissues within it.

Before wrongly concluding that loops of metal pose no risk in MRI, let's consider the case where a small break is present in the loop, as illustrated on the right side of Fig. 4. Note that the effect on the B field of the broken ring is not much different than if the ring were intact; however, the situation is much different for the E field and the resultant SAR in the region of the ring gap. The SAR is greatly elevated over the level seen in the rest of the tissue, with potential for significant local tissue damage. The importance of avoiding loops containing metal was shown by Bennet et al, who demonstrated significant heating in a metallic radiosurgery head frame at the tips of screws that clamp the frame to the head.⁷³ Loops of cables that come in contact with the body also have the potential to cause burns and should be avoided.

Although a less likely scenario, there is also the potential that a loop-containing implanted device might act as a

circuit in resonance,^{72,74,75} in which case a very significant amount of energy may be transferred, possibly resulting in destruction of the device and damage to surrounding tissue. An unblanked receive coil would be an example.⁷⁶

The Antenna Effect

The mechanism for RF heating discussed to this point has only involved the generation of current via induction in conductive loops. Straight wires (not bent into loops) can also pose a significant hazard and serious injury has resulted when they come in contact with the RF field and are subjected to the so-called antenna effect.

From antenna theory, it is known that currents can be induced in a conductive wire when excited by an incident E field oriented parallel to the direction of the wire. This theory has been invoked when explaining the observation that significant heating may be produced at the tips of wires exposed to the RF field in MRI. This is a resonant phenomenon in the sense that the length of the wire must be such as to support the formation of standing waves. Typically, wire lengths of a half wavelength are most likely to result in the maximum heating. The speed of light in a void is 3×10^8 m/s, meaning that a wave with $f = 127.7$ million oscillations per second would cover 2.35 meters per oscillation, which gives about 1.17 meters for a half wavelength. However, RF waves in MRI do not travel in a void and one must take into account the relative permittivity of tissue, $\epsilon_r = 80$. The half wavelength in tissue is reduced compared

to its value in the void by $\sqrt{\epsilon_r}$ down to about 13 cm here. The conductivity of tissues also comes into play and brings the half wavelength value even further down, for example, close to 12 cm if one assumes a conductivity of 0.5 S/m. Thus, in a 3T scanner ($f = 127.7$ MHz), an implanted wire in the range of 12 cm in length should be especially worrisome, although, given variability in the electrical properties of different tissues and uncertainty in estimation of wavelengths, one should not assume there will be no heating based on the length of the wire alone. Other factors, such as how the wire is terminated, have also been shown to be important in this regard.^{77,78}

The plot in Fig. 5 demonstrates the significant effect of wire length on heating in the RF field. The results of simulations with conductive wires embedded in tissue-like material show that SAR at the ends of the wires is maximized at a length of 12 cm, the half wavelength at $f = 127.7$ MHz. It is important to note that there is no significant heating of the metallic wires themselves,⁷⁹ as their high conductivity allows them to carry currents without significant resistance. However, biological tissues in immediate proximity with the wire do not have the benefit of such high conductivity and may experience significant heating, in particular, tissues that are close to the wire tips. The SAR image in Fig. 5 illustrates a highly localized energy deposition in the conductive medium near the ends of the 12-cm wires, where electric field variations are largest.

Localized SAR amplification has been predicted by simulation⁸⁰ and extrapolated from experiment⁸¹ to 10,000-fold or more; thus, even with relatively low RF input power, temperatures can rise rapidly. Indeed, significant temperature increases from 20–60°C have been recorded in experiments with a variety of devices that include wires; deep brain stimulators,^{82,83} vagus nerve stimulators,⁸⁴ pacemakers,^{77,85,86} guide wires,^{87,88} and EEG electrodes.⁸⁹ Temperatures exceeding 60°C were recorded in copper wires of resonant length at 1.5T.⁷² An incident ascribed to action of the antenna effect in an ECG lead resulted in a fire in 1.5T system and patient burns.⁹⁰

In addition to wire length and terminal conditions, position and orientation of the wire have also been shown to be significant.⁹¹ This is demonstrated by simulation results shown in Fig. 5 where half-wavelength wires (12 cm) were placed as indicated by the dashed white lines. Two wires oriented in the z -direction were placed as shown, yet only the wire near the edge of the phantom showed any significant energy deposition. There is no evidence of elevated SAR for the wire placed in the center of the phantom. This is because there is no significant z -component of \mathbf{E} at the center. Also, of the wires oriented in the y -direction, only the wire at the edge of the phantom caused a significant elevation in SAR, because this is where the \mathbf{E} field had a significant y -component.

An intuitive explanation for the antenna effect is that an incident \mathbf{E} field of appropriate wavelength and oriented along the length of the wire forces current back and forth coherently along the conductive metal wire. Driven by current, the wire then reradiates, as, for example, a dipole antenna. More in-depth analysis proceeds by direct application of Maxwell's equations, yielding Hallen's or Pocklington's integral equations whose solution, given the incident field, allows for the calculation of the current distribution on the wire and the radiated field pattern.^{88,92–95} Other approaches such as treating wires as transmission lines using a lumped-element model have been employed to estimate the current distribution along the wire.^{96,97}

MRI has also been used to estimate the induced currents by measuring their effect on the B_1 field^{98–100} or to directly estimate SAR via MRI-based temperature mapping.^{101,102} Direct measurement of induced currents with special sensors has also been employed to study the impact of wire configuration.^{103,104}

The Gradient Fields

Gradient coils in MRI systems are used to encode spatial information by adding a relatively small component to the B_0 field that varies linearly with position (and thus introducing a small spatially dependent variation in the Larmor frequency). In today's systems, spatial gradients of around 40 mT/m (or 4 G/cm) are common, and some newer commercial systems can go as high as 80 mT/m. Assuming an imaging field-of-view (FOV) of 50 cm, a 40 mT/m gradient set produces a maximum magnetic field strength of 10 mT (100 G) at the edges of the FOV. The magnitude of the fields produced by the gradient coils is around 3 orders of magnitude stronger than magnitude of the fields produced by RF coils, but between 2 and 3 orders of magnitude less than the static magnetic field. With slew rates of 200 T/m/s, the orientation of these fields can be reversed in times less than 1 millisecond. Compared to the static field and the RF field, the gradient fields are intermediate both in terms of strength and frequency of their temporal variation.

While forces due to the magnetic field were the key source of risk for the static field, and the generation of currents via magnetic induction was the key source of risk of the RF field, both forces and magnetic induction come into play when considering the safety of the gradient fields. How these issues are manifested, however, is quite different in the case of the gradients.

The problem of magnetic forces with reference to gradient coils is not one of keeping ferromagnetic objects away from the fields. For example, applying Eq. 3 for a saturated iron object ($B_s = 2.5$ T) and assuming a maximum imaging gradient field of 40 mT/m gives a force ratio of 1, about 2 orders of magnitude lower than what the object would be subjected to by the spatial gradient of the static field

discussed previously. For the gradients, as we will see below, the problem is instead the ear-damaging hammering caused by physical movement of the current-carrying conductors of the gradient coils as they interact with the static magnetic field.

The problem of the induction of eddy currents is not the associated heating, as it is with the RF field. For example, when Eq. 10 is used to calculate the SAR at the periphery of a body of radius of 20 cm where the maximum gradient field strength would be 8 mT (assuming 40 mT/m gradients), we obtain a SAR due to gradient switching (at 1 KHz) of only 0.006 W/kg, compared to 6.5 W/kg calculated for the RF field strength of 2 μ T. Instead of tissue heating, for gradients, the major concern is nerve, muscle, and other sensitive tissue stimulation that may result from the electric fields associated with the induced currents. This will be discussed in more detail below.

It was noted in an earlier section that charges moving through a magnetic field experience a force, the Lorentz force, proportional to velocity and the strength of the field (Eq. 7). The Lorentz force acting on metal current carrying conductors can be very large even for moderate currents. Hundreds of amperes may flow through gradient coils, resulting in enormous forces on the coil elements. Consider the example of a copper wire, 6 mm in diameter, carrying 100 amps, through a 3T magnetic field. From Eq. 7 it is readily derived that the force on the wire is equal to the product of the wire length, the current, and the magnetic field strength. Dividing this force by the weight of the wire we find that the Lorentz force on the wire relative to the gravitational force is over 120. This is comparable to the force ratio we found for ferromagnetic objects when in the region of the maximum spatial gradient of the MRI field. It is easy to see, therefore, how it is that the rapid switching of such large currents and the accompanying rapid reversal of the direction of the enormous Lorentz forces results in the loud banging sounds,^{105,106} the levels of which can easily exceed 130db in modern MRI systems.^{107,108} Temporary hearing loss was reported in early studies even with relatively low-field systems,¹⁰⁹ and guidelines have been established in the intervening years to protect exposed persons from permanent hearing damage.¹⁰⁸ Today, hearing protection is considered mandatory during any MRI procedure in order to reduce acoustic noise to safe levels.

Nerve and cardiac tissue stimulation due to rapidly switching gradients represent yet another source of concern.¹¹⁰ The mechanism by which stimulation occurs has been studied extensively.^{16,20,110} As discussed in previous sections, according to Faraday's law time-varying magnetic fields induce an EMF around a closed circuit proportional to the time rate of change of the total magnetic flux through the surface enclosed by the circuit. Given the rate of change in the gradient field, dB/dt , with the maximum

occurring at the periphery of an FOV of radius, R , the maximum induced field, E is given by the product of $R/2$ and dB/dt (ie, this result is obtained from Eq. 10 if one substitutes dB/dt for $2\pi f B_p$ assuming a sinusoidal variation of the gradient field with B_p being the peak magnitude). In order to achieve nerve stimulation, there is a threshold electric field strength, E_s , which is equal to $E_r (1 + \tau_c/\tau_d)$, where τ_d is the duration of the stimulation, E_r (called the rheobase) is the minimum E_r necessary to cause stimulation, and τ_c (called the chronaxie) is a reference stimulation time.

Values for both the rheobase and the chronaxie are obtained through fits performed on experimental data.¹¹¹ From simple assumptions about the geometry of the subject, a curve of dB/dt versus stimulus duration (gradient ramp time) can be obtained to determine if specific ramp durations are likely to cause nerve stimulation. Examination of these curves will reveal that peripheral nerve stimulation (PNS) is well within the capability of even older MRI systems.¹¹² While uncomfortable and possibly painful, PNS does not represent a grave threat. Cardiac stimulation, however, could have serious consequences and must therefore be considered. Fortunately, even with a very high dB/dt of 100 T/s, and maximum gradient amplitude of 80 mT/m on the newest commercial MRI systems, ramp times to reach peak are well below threshold values to cause cardiac stimulation.¹⁶ However, cardiac stimulation remains theoretically possible on some research systems outfitted with 300 mT/m gradients¹¹³ and special care must be exercised in such an environment.

In addition to the effects of switching gradient fields discussed above, interaction with implanted devices containing metals must also be carefully considered.¹¹⁴ In pacemakers, gradient field switching could possibly induce currents that might create competitive pacing, with the potential of causing life-threatening arrhythmias.^{115–117} Unintended electrical stimulation of tissue due to induction of currents on the leads of other active implants such as neurological stimulators could be another concern.¹¹⁸ Induced currents from gradient switching may also cause heating of devices containing metal components^{119,120} or they may generate a significant magnetic moment and cause vibration of devices as gradients are switched.¹²¹ Although less of a safety concern than interactions with the B_0 or RF fields, the switching of gradient fields should nevertheless be considered when evaluating devices for potential damaging interactions.

Discussion

In this article we aimed to explain how the large static magnetic field, the rapidly switched gradient fields, and the RF electromagnetic field present in MRI interact with human tissues and artificial metal objects. With regard to all potential interactions with biological systems, the present review

of necessity only scratched the surface. We have mostly limited ourselves to those interactions that are known to represent serious safety hazards in the context of today's MRI. Although we have included some limited discussion of exposure limits to these fields, an in-depth treatment is beyond the scope of this review and, for this the reader is directed to other sources.^{40,122}

In focusing exclusively on the hazards associated with MRI we have risked creating the impression that there is little that can be done about any of it. Fortunately, one constant rule about technological development is that, once a problem is identified, it may be only a matter of time before either a solution or a work-around can be found. And so it is too with MRI. The problem of heating due to the RF field, especially with regard to the interaction with implanted devices, is a good case in point. For example, a variety of techniques have been developed to defeat the antenna effect, by engineering wires and cables to be safer,^{123–127} or making changes to the RF transmit.^{128–131} More general solutions to the SAR problem have involved pulse sequence and RF pulse modifications.^{132–135} Engineering solutions have also been developed to address other safety-related issues such as reducing or buffering the noise produced by MRI gradient switching^{136,137} and developing detection systems to help keep ferromagnetic implants out of the MRI.^{138,139}

The central components of the imager are the subsystems that generate the magnetic fields essential to the production of MR images. Enormous energies go into producing these fields; hence, the potential dangers to life within them. MRI is known as a safe imaging modality because it does not require the use of ionizing radiation and, with proper care and management, the exquisite MR images we have come to expect can indeed be obtained safely. Understanding the physics underlying the risks in MRI is a key component for proper care and management, and it is with this goal in mind that we offer this work.

References

- Saunders RD, Smith H. Safety aspects of NMR clinical imaging. *Br Med Bull* 1984;40(2):148–154.
- Gangarosa RE, Minnis JE, Nobbe J, Praschan D, Genberg RW. Operational safety issues in MRI. *Magn Reson Imaging* 1987;5(4):287–292.
- Kanal E, Shellock FG, Talagala L. Safety considerations in MR imaging. *Radiology* 1990;176(3):593–606.
- Shellock FG. Radiofrequency energy-induced heating during MR procedures: a review. *J Magn Reson Imaging* 2000;12(1):30–36.
- Ahmed S, Shellock FG. Magnetic resonance imaging safety: implications for cardiovascular patients. *J Cardiovasc Magn Reson* 2001;3(3):171–182.
- Shellock FG, Crues JV. MR procedures: biologic effects, safety, and patient care. *Radiology* 2004;232(3):635–662.
- Stecco A, Saponaro A, Carriero A. Patient safety issues in magnetic resonance imaging: state of the art. *Radiol Med* 2007;112(4):491–508.
- Durbridge G. Magnetic resonance imaging: fundamental safety issues. *J Orthop Sports Phys Ther* 2011;41(11):820–828.
- Kathiravan S, Kanakaraj J. A review on potential issues and challenges in MR imaging. *ScientificWorldJournal*. 2013;2013:783715.
- Tsai LL, Grant AK, Morteale KJ, Kung JW, Smith MP. A practical guide to MR imaging safety: what radiologists need to know. *Radiographics* 2015;35(6):1722–1737.
- Bottomley PA, Andrew ER. RF magnetic field penetration, phase shift and power dissipation in biological tissue: implications for NMR imaging. *Phys Med Biol* 1978;23(4):630–643.
- Bottomley PA, Edelstein WA. Power deposition in whole-body NMR imaging. *Med Phys* 1981;8(4):510–512.
- Schenck JF. The role of magnetic susceptibility in magnetic resonance imaging: MRI magnetic compatibility of the first and second kinds. *Med Phys* 1996;23(6):815–850.
- Schaefer DJ. Safety aspects of radiofrequency power deposition in magnetic resonance. *Magn Reson Imaging Clin N Am* 1998;6(4):775–789.
- Price RR. The AAPM/RSNA physics tutorial for residents. MR imaging safety considerations. *Radiological Society of North America. Radiographics* 1999;19(6):1641–1651.
- Schaefer DJ, Bourland JD, Nyenhuis JA. Review of patient safety in time-varying gradient fields. *J Magn Reson Imaging* 2000;12(1):20–29.
- Schenck JF. Safety of strong, static magnetic fields. *J Magn Reson Imaging* 2000;12(1):2–19.
- Formica D, Silvestri S. Biological effects of exposure to magnetic resonance imaging: an overview. *Biomed Eng Online* 2004;Apr 22;3:11.
- Schenck JF. Physical interactions of static magnetic fields with living tissues. *Prog Biophys Mol Biol* 2005;87(2–3):185–204.
- Glover PM. Interaction of MRI field gradients with the human body. *Phys Med Biol* 2009;54(21):R99–R115.
- Lorrain P, Corson DR, Lorrain F. *Electromagnetic fields and waves*, 3rd edition. New York: W.H. Freeman; 1988.
- Hayt WH, Buck JA. *Engineering electromagnetics*, 8th edition. New York: McGraw Hill; 2012.
- Coey JMD. *Magnetism and magnetic materials*. Cambridge, UK: Cambridge University Press; 2013.
- Elsherbeni A, Demir V. *The finite-difference time-domain method for electromagnetics with MatLab simulations*. Raleigh, NC: SciTech Publishing; 2009.
- Gray T. Periodictable.com. Available at <http://www.periodictable.com>. Accessed April 18, 2017.
- Berry MV, Geim AK. Of flying frogs and levitrons. *Eur J Phys* 1997;18:307–313.
- American Society for Testing and Materials (ASTM) International. ASTM F2052-15: Standard Test Method for Measurement of Magnetically Induced Displacement Force on Medical Devices in the Magnetic Resonance Environment. West Conshohocken, PA: ASTM International; 2015.
- American Society for Testing and Materials (ASTM) International. ASTM F2213-06(2011): Standard Test Method for Measurement of Magnetically Induced Torque on Medical Devices in the Magnetic Resonance Environment. West Conshohocken, PA: ASTM International; 2011.
- Some Physics Insights. Force and torque on a small magnetic dipole. Available at http://www.physicsinsights.org/force_on_dipole_1.html. Accessed April 18, 2017.
- Haus H, Melcher JR. *Electromagnetic fields and energy*. Forces on microscopic electric and magnetic dipoles (Section 11.8). Available at http://web.mit.edu/6.013_book/www/book.html. Accessed April 18, 2017.
- Budinger TF, Bird MD, Frydman L, et al. Toward 20T magnetic resonance for human brain studies: Opportunities for discovery and neuroscience rationale. *MAGMA* 2016;29(3):617–639.
- Keltner JR, Roos MS, Brakeman PR, Budinger TF. Magneto-hydrodynamics of blood flow. *Magn Reson Med* 1990;16(1):139–149.

33. Kinouchi Y, Yamaguchi H, Tenforde TS. Theoretical analysis of magnetic field interactions with aortic blood flow. *Bioelectromagnetics* 1996;17(1):21–32.
34. Martin V, Drochon A, Fokapu O, Gerbeau JF. Magneto-hemodynamics in the aorta and electrocardiograms. *Phys Med Biol* 2012;57(10):3177–3195.
35. Laudon MK, Webster JG, Frayne R, Grist TM. Minimizing interference from magnetic resonance imagers during electrocardiography. *IEEE Trans Biomed Eng* 1998;45(2):160–164.
36. Park H, Park Y, Cho S, Jang B, Lee K. New cardiac MRI gating method using event-synchronous adaptive digital filter. *Ann Biomed Eng* 2009;37(11):2170–2187.
37. Buchenberg WB, Mader W Hoppe G, et al. In vitro study to simulate the intracardiac magnetohydrodynamic effect. *Magn Reson Med* 2015;74(3):850–857.
38. Crozier S, Trakic A, Wang H, Liu F. Numerical study of currents in workers induced by body-motion around high-ultrahigh field MRI magnets. *J Magn Reson Imaging* 2007;26(5):1261–1277.
39. Wang H, Takic A, Liu F, Crozier S. Numerical field evaluation of healthcare workers when bending towards high-field MRI magnets. *Magn Reson Med* 2008;59(2):410–422.
40. International Commission on Non-Ionizing Radiation Protection. ICNIRP Guidelines for limiting exposure to time-varying electric, magnetic and electromagnetic fields (up to 300GHz). *Health Phys* 1998;74(4):494–522.
41. Condon B, Hadley DM. Potential MR hazard to patients with metallic heart valves: the Lenz effect. *J Magn Reson Med* 2000;12(1):171–176.
42. Golestanirad L, Dlala E, Wright G, Mosig JR, Graham SJ. Comprehensive analysis of Lenz effect on the artificial heart valves during magnetic resonance imaging. *Prog Electromagn Res* 2012;128:1–17.
43. Hand JW. Modelling the interaction of electromagnetic fields (10 MHz–10 GHz) with the human body: methods and applications. *Phys Med Biol* 2008;53(16):R243–286.
44. Collins CM. Numerical field calculations considering the human subject for engineering and safety assurance in MRI. *NMR Biomed* 2009;22(9):919–926.
45. Hartwig V, Vanello N, Giovannetti G, Lombardi M, Landini L, Sartarelli MF. A novel tool for estimation of magnetic resonance occupational exposure to spatially varying magnetic fields. *MAGMA* 2011;24(6):323–330.
46. Hartwig V. Engineering for safety assurance in MRI: analytical, numerical and experimental dosimetry. *Magn Reson Imaging*; 2015 33(5):681–689.
47. Collins CM, Wang Z. Calculation of radiofrequency electromagnetic fields and their effects in MRI of human subjects. *Magn Reson Med* 2011;65(5):1470–1482.
48. Alon L, Deniz CM, Carluccio G, Brown R, Sodickson DK, Collins CM. Effects of anatomical differences on electromagnetic fields, SAR, and temperature change. *Concepts Magn Reson Part B Magn Reson Eng* 2016;46(1):8–18.
49. Collins CM, Li S, Smith MB. SAR and B1 field distributions in a heterogeneous human head model within a birdcage coil. Specific energy absorption rate. *Magn Reson Med* 1998;40(6):847–856.
50. Gandhi OP, Chen XB. Specific absorption rates and induced current densities for an anatomy-based model of the human for exposure to time-varying magnetic fields of MRI. *Magn Reson Med* 1999;41(4):816–823.
51. Collins CM, Smith MB. Calculations of B(1) distribution, SNR, and SAR for a surface coil adjacent to an anatomically-accurate human body model. *Magn Reson Med* 2001;45(4):692–699.
52. Collins CM, Smith MB. Spatial resolution of numerical models of man and calculated specific absorption rate using the FDTD method: a study at 64 MHz in a magnetic resonance imaging coil. *J Magn Reson Imaging* 2003;18(3):383–388.
53. Stuchly MA, Abrishamkar H, Strydom ML. Numerical evaluation of radio frequency power deposition in human models during MRI. *Conf Proc IEEE Eng Med Biol Soc* 2006;1:272–275.
54. Murbach M, Cabot E, Neufeld E, et al. Local SAR enhancements in anatomically correct children and adult models as a function of position within 1.5 T MR body coil. *Prog Biophys Mol Biol* 2011;107(3):428–433.
55. Murbach M, Neufeld E, Kainz W, et al. Whole-body and local RF absorption in human models as a function of anatomy and position within 1.5T MR body coil. *Magn Reson Med* 2014;71(2):839–845.
56. Gosselin MC, Neufeld E, Moser H, et al. Development of a new generation of high-resolution anatomical models for medical device evaluation: the Virtual Population 3.0. *Phys Med Biol* 2014;59(18):5287–5303.
57. Katscher U, Voigt T, Findelee C, Vernickel P, Nehrke K, Dössel O. Determination of electric conductivity and local SAR via B1 mapping. *IEEE Trans Med Imaging* 2009;28(9):1365–74.
58. Zhang X, Zhu S, He B. Imaging electric properties of biological tissues by RF field mapping in MRI. *IEEE Trans Med Imaging* 2010 Feb;29(2):474–481.
59. Zhang X, Van de Moortele PF, Liu J, Schmitter S, He B. Quantitative prediction of radio frequency induced local heating derived from measured magnetic field maps in magnetic resonance imaging: A phantom validation at 7T. *Appl Phys Lett* 2014;105(24):244101.
60. Tiberi G, Costagli M, Biagi L, et al. SAR prediction in adults and children by combining measured B1+ maps and simulations at 7.0 Tesla. *J Magn Reson Imaging* 2016;44(4):1048–1055.
61. Yeung CJ, Atalar E. A Green's function approach to local rf heating in interventional MRI. *Med Phys* 2001;28(5):826–832.
62. Brix G, Seebass M, Hellwig G, Griebel J. Estimation of heat transfer and temperature rise in partial-body regions during MR procedures: an analytical approach with respect to safety considerations. *Magn Reson Imaging* 2002;20(1):65–76.
63. Collins CM, Liu W, Wang J, et al. Temperature and SAR calculations for a human head within volume and surface coils at 64 and 300 MHz. *J Magn Reson Imaging* 2004;19(5):650–656.
64. Wang Z, Lin JC, Vaughan JT, Collins CM. Consideration of physiological response in numerical models of temperature during MRI of the human head. *J Magn Reson Imaging* 2008;28(5):1303–1308.
65. Wang Z, Collins CM. Effect of RF pulse sequence on temperature elevation for a given time-average SAR. *Concepts Magn Reson Part B Magn Reson Eng* 2010;37B(4):215–219.
66. van Lier AL, Kotte AN, Raaymakers BW, Lagendijk JJ, van den Berg CA. Radiofrequency heating induced by 7T head MRI: thermal assessment using discrete vasculature or Pennes' bioheat equation. *J Magn Reson Imaging* 2012;35(4):795–803.
67. Ishihara Y, Watanabe H, Okamoto K, Kanamatsu T, Tsukada Y. Temperature monitoring of internal body heating induced by decoupling pulses in animal (13)C-MRS experiments. *Magn Reson Med* 2000;43(6):796–803.
68. Shapiro EM, Borthakur A, Shapiro MJ, Reddy R, Leigh JS. Fast MRI of RF heating via phase difference mapping. *Magn Reson Med* 2002;47(3):492–498.
69. Cline H, Mallozzi R, Li Z, McKinnon G, Barber W. Radiofrequency power deposition utilizing thermal imaging. *Magn Reson Med* 2004;51(6):1129–1137.
70. Wimmer R, Wider G. Real-time imaging of the spatial distribution of RF-heating in NMR samples during broadband decoupling. *J Magn Reson* 2007;187(2):184–192.
71. Cao Z, Oh S, Otazo R, Sica CT, Griswold MA, Collins CM. Complex difference constrained compressed sensing reconstruction for accelerated PRF thermometry with application to MRI-induced RF heating. *Magn Reson Med* 2015;73(4):1420–1431.
72. Dempsey MF, Condon B, Hadley DM. Investigation of the factors responsible for burns during MRI. *J Magn Reson Imaging* 2001;13(4):627–631.
73. Bennett MC, Wiant DB, Gersh JA, Dolesh W, Ding X, Best RC, Bourland JD. Mechanisms and prevention of thermal injury from gamma radiosurgery headframes during 3T MR imaging. *J Appl Clin Med Phys* 2012;13(4):54–70.

74. Busch MH, Vollmann W, Grönemeyer DH. Finite volume analysis of temperature effects induced by active MRI implants: 2. Defects on active MRI implants causing hot spots. *Biomed Eng Online* 2006; May 26;5:35.
75. Ballweg V, Eibofner F, Graf H. RF tissue-heating near metallic implants during magnetic resonance examinations: an approach in the ac limit. *Med Phys* 2011;38(10):5522–5529.
76. Buchli R, Saner M, Meier D, Boskamp EB, Boesiger P. Increased RF power absorption in MR imaging due to RF coupling between body coil and surface coil. *Magn Reson Med* 1989;9(1):105–112.
77. Langman DA, Goldberg IB, Finn JP, Ennis DB. Pacemaker lead tip heating in abandoned and pacemaker-attached leads at 1.5 Tesla MRI. *J Magn Reson Imaging* 2011;33(2):426–431.
78. Mattei E, Gentili G, Censi F, Triventi M, Calcagnini G. Impact of capped and uncapped abandoned leads on the heating of an MR-conditional pacemaker implant. *Magn Reson Med* 2015;73(1):390–400.
79. Yeung CJ, Atalar E. RF transmit power limit for the barewire loopless catheter antenna. *J Magn Reson Imaging* 2000;12(1):86–91.
80. Yeung CJ, Susil RC, Atalar E. RF safety of wires in interventional MRI: using a safety index. *Magn Reson Med* 2002;47(1):187–193.
81. Mattei E, Triventi M, Calcagnini G, et al. Complexity of MRI induced heating on metallic leads: experimental measurements of 374 configurations. *Biomed Eng Online* 2008 Mar 3;7:11.
82. Rezaei AR, Finelli D, Nyenhuis JA, et al. Neurostimulation systems for deep brain stimulation: in vitro evaluation of magnetic resonance imaging-related heating at 1.5 Tesla. *J Magn Reson Imaging* 2002; 15(3):241–250.
83. Shrivastava D, Abosch A, Hanson T, et al. Effect of the extracranial deep brain stimulation lead on radiofrequency heating at 9.4 Tesla (400.2 MHz). *J Magn Reson Imaging* 2010;32(3):600–607.
84. Shellock FG, Begnaud J, Inman DM. Vagus nerve stimulation therapy system: in vitro evaluation of magnetic resonance imaging-related heating and function at 1.5 and 3 Tesla. *Neuromodulation*. 2006;9(3): 204–213.
85. Sommer T, Vahlhaus C, Lauck G, et al. MR imaging and cardiac pacemakers: in-vitro evaluation and in-vivo studies in 51 patients at 0.5 T. *Radiology* 2000;215(3):869–879.
86. Nordbeck P, Fidler F, Friedrich MT, et al. Reducing RF-related heating of cardiac pacemaker leads in MRI: implementation and experimental verification of practical design changes. *Magn Reson Med* 2012;68(6): 1963–1972.
87. Konings MK, Bartels LW, Smits HF, Bakker CJ. Heating around intravascular guidewires by resonating RF waves. *J Magn Reson Imaging* 2000;12(1):79–85.
88. Armenean C, Perrin E, Armenean M, Beuf O, Pilleul F, Saint-Jalmes H. RF-induced temperature elevation along metallic wires in clinical magnetic resonance imaging: influence of diameter and length. *Magn Reson Med* 2004;52(5):1200–1206.
89. Balasubramanian M, Wells WM, Ives JR, Britz P, Mulkern RV, Orbach DB. RF heating of gold cup and conductive plastic electrodes during simultaneous EEG and MRI. *Neurodiagn J* 2017;57(1):69–83.
90. Kugel H, Bremer C, Püschel M, et al. Hazardous situation in the MR bore: induction in ECG leads causes fire. *Eur Radiol* 2003;13(4):690–694.
91. Nordbeck P, Fidler F, Weiss I, et al. Spatial distribution of RF-induced E-fields and implant heating in MRI. *Magn Reson Med* 2008;60(2): 312–319.
92. Pictet J, Meuli R, Wicky S, van der Klink JJ. Radiofrequency heating effects around resonant lengths of wire in MRI. *Phys Med Biol* 2002; 47(16):2973–2985.
93. Rawle WD. The method of moments: A numerical technique for wire antenna design. In: *High Frequency Electronics*. February 2006;42–47.
94. Park SM, Kamondetdacha R, Nyenhuis JA. Calculation of MRI-induced heating of an implanted medical lead wire with an electric field transfer function. *J Magn Reson Imaging* 2007;26(5):1278–1285.
95. Bayjja M, Boussouis M, Amar Touhami N, Zeljami K. Comparison between solution of Pocklington's and Hallen's integral equations for thin wire antennas using method of moments and Haar wavelet. *Int J Innovation Appl Studies* 2015;12(4):931–942.
96. Nitz WR, Oppelt A, Renz W, Manke C, Lenhart M, Link J. On the heating of linear conductive structures as guide wires and catheters in interventional MRI. *J Magn Reson Imaging* 2001;13(1):105–114.
97. Acikel V, Atalar E. Modeling of radio-frequency induced currents on lead wires during MR imaging using a modified transmission line method. *Med Phys* 2011;38(12):6623–6632.
98. van den Bosch MR, Moerland MA, Lagendijk JJ, Bartels LW, van den Berg CA. New method to monitor RF safety in MRI-guided interventions based on RF induced image artefacts. *Med Phys* 2010;37(2):814–821.
99. Overall WR, Pauly JM, Stang PP, Scott GC. Ensuring safety of implanted devices under MRI using reversed RF polarization. *Magn Reson Med* 2010;64(3):823–833.
100. Griffin GH, Anderson KJ, Celik H, Wright GA. Safely assessing radio-frequency heating potential of conductive devices using image-based current measurements. *Magn Reson Med* 2015;73(1):427–441.
101. Ehses P, Fidler F, Nordbeck P, et al. MRI thermometry: Fast mapping of RF-induced heating along conductive wires. *Magn Reson Med* 2008;60(2):457–461.
102. Gensler D, Fidler F, Ehses P, et al. MR safety: fast T₁ thermometry of the RF-induced heating of medical devices. *Magn Reson Med* 2012; 68(5):1593–1599.
103. Nordbeck P, Weiss I, Ehses P, et al. Measuring RF-induced currents inside implants: Impact of device configuration on MRI safety of cardiac pacemaker leads. *Magn Reson Med* 2009;61(3):570–578.
104. Zanchi MG, Venook R, Pauly JM, Scott GC. An optically coupled system for quantitative monitoring of MRI-induced RF currents into long conductors. *IEEE Trans Med Imaging* 2010;29(1):169–178.
105. McJury MJ. Acoustic noise levels generated during high field MR imaging. *Clin Radiol* 1995;50(5):331–334.
106. Counter SA, Olofsson A, Grahn HF, Borg E. MRI acoustic noise: sound pressure and frequency analysis. *J Magn Reson Imaging* 1997;7(3):606–611.
107. Ravicz ME, Melcher JR, Kiang NY. Acoustic noise during functional magnetic resonance imaging. *J Acoust Soc Am* 2000;108(4):1683–1696.
108. Foster JR, Hall DA, Summerfield AQ, Palmer AR, Bowtell RW. Sound-level measurements and calculations of safe noise dosage during EPI at 3 T. *J Magn Reson Imaging* 2000;12(1):157–163.
109. Brummett RE, Talbot JM, Charuhas P. Potential hearing loss resulting from MR imaging. *Radiology* 1988;169(2):539–540.
110. Irnich W, Schmitt F. Magnetostimulation in MRI. *Magn Reson Med* 1995;33(5):619–623.
111. Recoskie BJ, Scholl TJ, Zinke-Allmang M, Chronik BA. Sensory and motor stimulation thresholds of the ulnar nerve from electric and magnetic field stimuli: implications to gradient coil operation. *Magn Reson Med* 2010;64(6):1567–1579.
112. Cohen MS, Weisskoff RM, Rzedzian RR, Kantor HL. Sensory stimulation by time-varying magnetic fields. *Magn Reson Med* 1990;14(2): 409–414.
113. McNab JA, Edlow BL, Witzel T, et al. The Human Connectome Project and beyond: initial applications of 300 mT/m gradients. *Neuroimage* 2013;80:234–245.
114. Buechler DN, Durney CH, Christensen DA. Calculation of electric fields induced near metal implants by magnetic resonance imaging switched-gradient magnetic fields. *Magn Reson Imaging* 1997; 15(10):1157–1166.
115. Irnich W, Irnich B, Bartsch C, Stertmann WA, Gufler H, Weiler G. Do we need pacemakers resistant to magnetic resonance imaging? *Europace* 2005;7(4):353–365.
116. Tandri H, Zviman MM, Wedan SR, Lloyd T, Berger RD, Halperin H. Determinants of gradient field-induced current in a pacemaker lead

- system in a magnetic resonance imaging environment. *Heart Rhythm* 2008;5(3):462–468.
117. Jung W, Zvereva V, Hajredini B, Jäckle S. Initial experience with magnetic resonance imaging-safe pacemakers : a review. *J Interv Card Electrophysiol* 2011;32(3):213–219.
 118. Bassen HI, Angelone LM. Evaluation of unintended electrical stimulation from MR gradient fields. *Front Biosci (Elite Ed)* 2012;4:1731–1742.
 119. Graf H, Steidle G, Schick F. Heating of metallic implants and instruments induced by gradient switching in a 1.5-Tesla whole-body unit. *J Magn Reson Imaging* 2007;26(5):1328–1333.
 120. El Bannan K, Handler W, Chronik B, Salisbury SP. Heating of metallic rods induced by time-varying gradient fields in MRI. *J Magn Reson Imaging* 2013;38(2):411–416.
 121. Graf H, Lauer UA, Schick F. Eddy-current induction in extended metallic parts as a source of considerable torsional moment. *J Magn Reson Imaging* 2006;23(4):585–590.
 122. International Commission on Non-Ionizing Radiation Protection. Guidelines on limits of exposure to static magnetic fields. *Health Phys* 2009;96(4):504–514.
 123. Bottomley PA, Kumar A, Edelstein WA, Allen JM, Karmarkar PV. Designing passive MRI-safe implantable conducting leads with electrodes. *Med Phys* 2010;37(7):3828–3843.
 124. Ladd ME, Quick HH. Reduction of resonant RF heating in intravascular catheters using coaxial chokes. *Magn Reson Med* 2000;43(4):615–619.
 125. Gray RW, Bibens WT, Shellock FG. Simple design changes to wires to substantially reduce MRI-induced heating at 1.5 T: implications for implanted leads. *Magn Reson Imaging* 2005;23(8):887–891.
 126. Weiss S, Vernickel P, Schaeffter T, Schulz V, Gleich B. Transmission line for improved RF safety of interventional devices. *Magn Reson Med* 2005;54(1):182–189.
 127. Negishi M, Abildgaard M, Laufer I, Nixon T, Constable RT. An EEG (electroencephalogram) recording system with carbon wire electrodes for simultaneous EEG-fMRI (functional magnetic resonance imaging) recording. *J Neurosci Methods* 2008;173(1):99–107.
 128. Eryaman Y, Akin B, Atalar E. Reduction of implant RF heating through modification of transmit coil electric field. *Magn Reson Med* 2011;65(5):1305–1313.
 129. Etezadi-Amoli M, Stang P, Kerr A, Pauly J, Scott G. Controlling radiofrequency-induced currents in guidewires using parallel transmit. *Magn Reson Med* 2015;74(6):1790–1802.
 130. Gudino N, Sonmez M, Yao Z, et al. Parallel transmit excitation at 1.5 T based on the minimization of a driving function for device heating. *Med Phys* 2015;42(1):359–371.
 131. Golestanirad L, Keil B, Angelone LM, Bonmassar G, Mareyam A, Wald LL. Feasibility of using linearly polarized rotating birdcage transmitters and close-fitting receive arrays in MRI to reduce SAR in the vicinity of deep brain stimulation implants. *Magn Reson Med* 2017;77(4):1701–1712.
 132. Brunner DO, Pruessmann KP. Optimal design of multiple-channel RF pulses under strict power and SAR constraints. *Magn Reson Med* 2010;63(5):1280–1291.
 133. Wu X, Akgün C, Vaughan JT, et al. Adapted RF pulse design for SAR reduction in parallel excitation with experimental verification at 9.4 T. *J Magn Reson* 2010;205(1):161–170.
 134. Sbrizzi A, Hoogduin H, Lagendijk JJ, Luijten P, Sleijpen GL, van den Berg CA. Fast design of local N-gram-specific absorption rate-optimized radiofrequency pulses for parallel transmit systems. *Magn Reson Med* 2012;67(3):824–834.
 135. Choli M, Blaimer M, Breuer FA, et al. Combined acquisition technique (CAT) for high-field neuroimaging with reduced RF power. *MAGMA* 2013;26(4):411–418.
 136. McJury M, Stewart RW, Crawford D, Toma E. The use of active noise control (ANC) to reduce acoustic noise generated during MRI scanning: some initial results. *Magn Reson Imaging* 1997;15(3):319–322.
 137. Alibek S, Vogel M, Sun W, et al. Acoustic noise reduction in MRI using Silent Scan: an initial experience. *Diagn Interv Radiol* 2014;20(4):360–363.
 138. Shellock FG, Karacozoff AM. Detection of implants and other objects using a ferromagnetic detection system: implications for patient screening before MRI. *Am J Roentgenol* 2013;201(4):720–725.
 139. Gianesin B, Zefiro D, Paparo F, et al. Characterization of ferromagnetic or conductive properties of metallic foreign objects embedded within the human body with magnetic iron detector (MID): Screening patients for MRI. *Magn Reson Med* 2015;73(5):2030–2037.